nature communications

Article

https://doi.org/10.1038/s41467-025-67876-1

Size-dependent translocation of polystyrene nanoplastics across biological barriers in mammals

Received: 22 October 2025

Accepted: 10 December 2025

Published online: 26 December 2025

Check for updates

Hong-Jie Zhang[1,5], Sicheng Li[2,5], Xin-Lei Wang[1], Ke-Da Zhang[1], Hai-Tao Fang[1], Xuan Wu[1], Ziyun Huang[1], Wei Jiang[1], Liuyan Yang[1], Qiao-Guo Tan[3], Bingcai Pan[1], Rong Ji[1] ✉, Ping Wang[2] ✉, Baoshan Xing[4] & Ai-Jun Miao[1] ✉

Nanoplastics (NPs) pose health concerns worldwide. However, robust quantitative data on their absorption, distribution, and excretion in mammals remain scarce. Here, we provide a comprehensive assessment of polystyrene (PS) NP biodistribution and elimination in rats using ^{14}C-radiolabeling, the most accurate and quantitative method available. Pregnant rats were exposed to ^{14}C-labeled 20 nm or 100 nm PS NPs (PS_{20} or PS_{100}) via oral gavage, intratracheal aerosolization, or intravenous injection, and tissue distribution and excretion were determined by radioactivity measurements. We found that PS NPs were exclusively excreted through faeces, irrespective of the exposure routes, without urinary elimination. Both PS_{20} and PS_{100} crossed multiple biological barriers, yet only PS_{20} reached the brain. Maternal transfer of PS_{20} occurred through both placenta and milk, while PS_{100} transferred solely via milk. A physiologically based toxicokinetic model further simulated accumulation kinetics across tissues. This study establishes the most comprehensive and reliable quantitative profile of PS NP biodistribution in mammals to date, revealing distinct size-dependent translocation patterns that provide a robust foundation for evaluating their health impacts.

Globally, over 6 billion metric tons of plastic waste had been generated by 2015, and estimates show a rise to ~12 billion tons by 2050[1]. Fragmentation of this waste[2,3] produces microplastics (MPs, 1–5000 μm) and nanoplastics (NPs, <1 μm) that are potentially hazardous to human health[4–6]. Recent estimates suggest that humans ingest ~0.1–5.0 g of these plastic particles weekly[7] and inhale ~6.5–9.0 μg/kg body weight daily[8]. MPs and NPs intentionally produced for various applications such as drug carriers[9] and those released from disposable plastic infusion tubes and bags[10] also find their way into our bloodstream. Such significant exposures from different routes mean high risks and therefore, a quantitative understanding of the absorption, distribution, and excretion of these plastic particles through various exposure pathways is critical and urgent[6].

Despite extensive research on the biodistribution and elimination of MPs and NPs, ongoing debate persists regarding their ability to cross mammalian biological barriers. For instance, while some studies report no systemic uptake (i.e., no barrier traversal) of MPs and NPs following oral exposure[11,12], others have detected them in multiple organs[13,14]. Moreover, particles as large as several micrometers have been reported to traverse the blood-brain barrier (BBB)[15], the urinary

[1]State Key Laboratory of Water Pollution Control and Green Resource Recycling, School of the Environment, Nanjing University, Nanjing, Jiangsu Province, China. [2]Changping Laboratory, Beijing, China. [3]Key Laboratory of the Coastal and Wetland Ecosystems of Ministry of Education, College of the Environment and Ecology, Xiamen University, Xiamen, Fujian, China. [4]Stockbridge School of Agriculture, University of Massachusetts, Amherst, MA, USA. [5]These authors contributed equally: Hong-Jie Zhang, Sicheng Li. ✉e-mail: ji@nju.edu.cn; pwang@cpl.ac.cn; miaoaj@nju.edu.cn

system barriers[16], and the placental barrier[17], even though these barriers are known to be permeable only to nano-sized particles[18]. These discrepancies may arise from the use of fluorescence labeling techniques, which can introduce artifacts due to dye leaching[19]. Similar issues are encountered with non-carbon isotope[20–22] and heavy metal[23,24] labeling methods. In addition, contamination of MPs or NPs during sample collection and digestion, as well as matrix interference, cannot be ruled out. Consequently, current findings are largely qualitative, and possible methodological artifacts may affect their validity.

Here, we accurately quantify the absorption, distribution, and excretion of 20 nm and 100 nm polystyrene (PS_{20} and PS_{100}) NPs in pregnant Sprague Dawley (SD) rats, employing ^{14}C-labeling alongside verification techniques such as gel permeation chromatography (GPC) and stimulated Raman scattering microscopy (SRS). We focus on NPs, whose smaller size compared to MPs may lead to greater health impacts[23]. PS, as a representative of conventional polymers, has been most frequently examined. By labeling the PS backbone with ^{14}C isotope[25–28], we exclude the possibility of label leaching, making ^{14}C labeling the most reliable method for quantifying the tissue distribution and elimination of PS NPs. To explore the effects of exposure routes on the biodistribution of PS NPs, rats are administered radiolabeled particles via oral gavage (OG), intratracheal aerosolization (ITA), or intravenous injection (IVI). Their distribution in the urine, faeces, gastrointestinal (GI) tract, lungs, blood, thoracic and abdominal aorta, liver, spleen, brain, heart, kidneys, residual tissues, and maternal transfer via placenta and breast milk is quantified and then simulated by a physiologically based toxicokinetic (PBTK) model. Detailed information about the comparable physicochemical properties of ^{14}C- and their unlabeled counterparts is provided in Supplementary Text and Fig. S1.

Results and Discussion

Potential elimination of PS NPs through urine and faeces

One day after administering 0.84 mg of ^{14}C-labeled PS NPs (1.9×10^{14} particles of PS_{20} and 1.5×10^{12} particles of PS_{100}) to each rat, a notable amount of radioactivity was detected in the urine (Fig. 1a). However, the daily urinary excretion of ^{14}C declined rapidly over time, as indicated by the quickly decreasing slope of the cumulative percentage curve. After 5 days, no more radioactivity was detected in the urine and the total amount of ^{14}C excreted through urine accounted for 0.08–0.21% of the initial dose. GPC results of urine further indicated that the radioactivity primarily stemmed from small molecules resembling the residual mono- and oligomers (i.e., ^{14}C-labeled styrene monomer and short oligomers remaining from PS NP synthesis) present in the PS NP preparation (Fig. S2). As PS NPs are relatively inert, the urination results suggest that the residual mono- and oligomers adsorbed on the surface of PS NPs (0.3–0.4% of the total dose) were not completely removed by diafiltration. These residual mono- and oligomers rapidly dissociated from the PS NPs and were excreted in urine, regardless of the location of the PS NPs in the rats. Despite significant renal accumulation of PS NPs (Fig. S3a), their absence in the urine implies that neither PS_{20} nor PS_{100} is excreted via urine, likely due to the physiological pore size limit (<10 nm) for urinary system barriers[29,30].

In contrast to urine, a substantial proportion of PS NPs was excreted through faeces, as verified by the same MW distribution of the ^{14}C-labeled compounds in faeces and PS NPs themselves (Fig. S2). Within the first day, the faecal excretion of PS NPs administered via OG was the most significant, constituting 49.7–62.2% of the initial dose, followed by ITA with 6.94–22.2%, and IVI with only 0.35% (Fig. 1b). Initially high, daily faecal excretion of PS NPs from OG and ITA declined sharply until day 5. Afterward, there was a significant increase, followed by a gradual decrease or stabilization. This phenomenon suggests biphasic excretion of both PS NPs from different compartments within the rats. In contrast, the daily excretion of PS NPs via IVI remained relatively constant, with the slope of the cumulative percentage curve unchanged over the 19-day period. Moreover, a higher percentage of PS_{100} was excreted through faeces following OG compared to PS_{20}, whereas the opposite trend was observed for ITA and IVI ($p < 0.05$, two-way ANOVA).

The observed higher faecal excretion of PS_{100} compared to PS_{20} following OG (Fig. 1b) suggests a reduced absorption of PS_{100} through

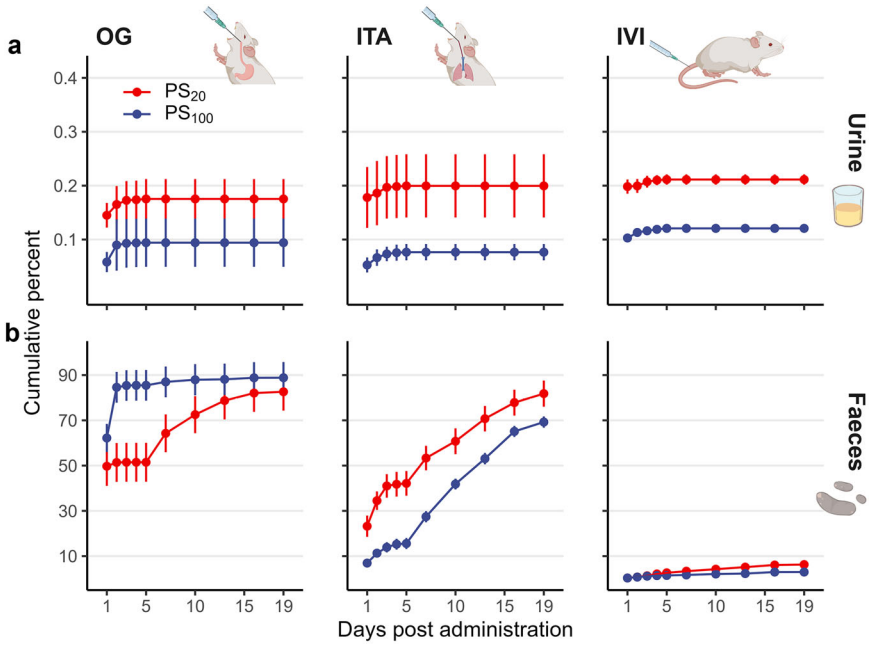

Fig. 1 | Potential elimination of PS NPs through urine and faeces. The cumulative percentage of ^{14}C in the **a** urine and **b** faeces on days 1–19 post the administration of PS_{20} or PS_{100} via oral gavage (OG), intratracheal aerosolization (ITA), or intravenous injection (IVI). All data (mean ± standard deviation, $n = 3$) are displayed as the cumulative percentage of ^{14}C radioactivity in the specific excreta normalized to the total radioactivity of ^{14}C administered to the rats. All data points include error bars, some of which are small and obscured by the data point symbols.

the GI tract. The rapid faecal excretion of PS NPs administered via ITA indicates that a portion of the particles in the lungs were efficiently cleared by mucociliary transport up the airway, eventually into the pharynx and the GI tract[31]. Further, the mucociliary clearance rate for PS_{20} is higher than that for PS_{100}, indicating that not only micrometer-sized particles but also extremely small particles (e.g., less than 100 nm) can be readily cleared. The minimal but relatively constant faecal excretion of PS NPs following IVI is attributable to the challenges faced by the NPs in transferring from the bloodstream to the GI tract.

Distribution of PS NPs in different tissues and blood

Due to the rapid faecal excretion following OG, with PS_{100} being excreted more rapidly than PS_{20}, only 40.8% (34.6%) of the initial PS_{20} (PS_{100}) doses retained in the GI tract 1 day post administration, decreasing consecutively to 7.61% (3.73%) after 19 days (Fig. 2a). Following ITA, PS_{20} was more efficiently eliminated through mucociliary clearance than PS_{100}, leading to higher levels of PS_{20} in the GI tract (Fig. 2a). Specifically, a maximum value was observed on day 5, indicating that it takes time for PS NPs to transport from the lungs to the GI tract. In contrast to OG and ITA, PS NPs administered via IVI had the lowest overall presence in the GI tract (Fig. 2a). Furthermore, following IVI, the amount of PS_{20} in the GI tract was lower than that of PS_{100} ($p < 0.05$, two-way ANOVA), as PS_{20} was excreted more rapidly via faeces for this administration route (Fig. 1b). The MW distribution of the ^{14}C-labeled compounds accumulated in the GI tract and other tissues or body fluids was the same as that of PS NPs themselves (Fig. S2), confirming the presence of PS NPs.

Despite the considerable faecal excretion of PS NPs administered via ITA, the majority (73.7–90.8%) accumulated in the lungs within the first day post-administration, with a subsequent decline over time (Fig. 2b). The temporal reduction of PS NPs in the lungs is attributed to clearance mechanisms such as mucociliary transport, phagocytosis by alveolar macrophages, and lymphatic transport[32]. Although lower than ITA, significant lung accumulation was observed for PS NPs administered through IVI (0.08–1.69%) and OG (0.007–0.16%). The proportions obtained herein seem low. But they were orders of magnitude higher than the limit of quantification (2.8×10^{-4})% and represented a huge number (1.1×10^{8}–3.2×10^{12}) of PS NPs. Across all administration routes, a greater overall proportion of PS_{100} was retained in the lungs compared to PS_{20} ($p < 0.05$, two-way ANOVA), which may be due to the more rapid transport of PS_{20} from lungs to faeces (Fig. 1b).

Although PS NPs were introduced directly to the bloodstream in the IVI treatment, only a minuscule proportion of PS_{20} (0.27%) and PS_{100} (0.66%) remained in the blood 1 day post administration (Fig. 2c). This finding implies that PS NPs may be rapidly sequestered from the blood into certain tissues (e.g., liver and spleen), due to the high rate of blood circulation in rats[33]. Additionally, a significant amount of PS NPs was also adsorbed on blood vessels, likely through a combination of non-specific physical interactions (such as van der Waals forces, electrostatic and hydrophobic interactions) and hemodynamic effects that enhance particle-endothelium contact. For instance, 6.15–16.3% of PS_{20} and 0.004–10.0% of PS_{100} were adsorbed on the thoracic and abdominal aorta within 19 days post-IVI (Fig. 2d). This adsorption may explain the previously reported presence of NPs in carotid artery plaques of patients with asymptomatic carotid artery disease[34]. Compared to IVI, blood concentrations of PS NPs (≤ 0.08%) were significantly ($p < 0.05$, two-way ANOVA) lower following OG and ITA administration, as PS NPs from these two routes needed to cross biological barriers (e.g., intestinal and blood-air barriers) before entering the blood. The low levels of PS NPs in the blood suggest a primary role for the circulatory system in transporting these particles rather than in their accumulation.

In line with the swift removal of PS NPs from the bloodstream post-IVI, a substantial fraction accumulated in the liver, with 55.3% of PS_{20} and 50.5% of PS_{100} present 1 day post administration, levels that significantly ($p < 0.05$, one-way ANOVA) changed to 19.6% and 73.4% by day 19 (Fig. 2e). The decreasing trend for PS_{20} may be attributed to their redistribution within the animal, supported by their time-dependent increase in the spleen (Fig. 2f), thoracic and abdominal aorta (Fig. 2d), and residual tissues (Fig. S3b). For instance, the proportion of PS_{20} in the spleen increased from 22.3% to 30.4% over 19 days post-IVI (Fig. 2f). In contrast, the increasing levels of PS_{100} and their greater accumulation in the liver compared to PS_{20} at later time points suggest weaker penetration and transport ability for PS_{100}[18,35]. The distinct difference in hepatic accumulation between PS_{20} and PS_{100} explains their opposing trend over time in the spleen (Fig. 2f), thoracic and abdominal aorta (Fig. 2d), and residual tissues (Fig. S3b). The hepatic accumulation of PS NPs from IVI was further verified by SRS (Fig. 3), according to their specific aromatic C-H stretching vibrations at 3061 cm^{-1}. For OG and ITA routes, the liver contained much lower proportions of PS NPs than IVI, preventing visualization by SRS. However, significant accumulation of both PS_{20} and PS_{100} administered through these two routes in the liver indicates that they can cross the intestinal and blood-air barriers. Absorption in the GI tract likely occurs through endocytosis by microfold cells in Peyer's patches[36] and enterocytes in the villous epithelium[18,37]. The significant extrapulmonary translocation of PS NPs administered via ITA to the liver (Fig. 2e), with PS_{20} exhibiting greater ($p < 0.05$, t-test) overall translocation than PS_{100}, indicated size-dependent translocation across the lung epithelium[31,38].

Detectable levels of PS_{20} were also found in the brain 1 day post administration, as verified by GPC (Fig. S2), representing 0.01%, 0.02%, and 0.03% of the initial dose from OG, ITA, and IVI, respectively (Fig. 2g). While PS_{20} were not detected in the brain after 5 days, a notable presence was observed again on day 19 post-administration, suggesting their repeated uptake into and clearance from the brain via the bloodstream, as evidenced by similar time-dependent variations in blood levels (Fig. 2c). In contrast, PS_{100} were not detected in the brain at any time point, regardless of the administration route. The blood-brain barrier BBB serves as a selective semi-permeable interface that shields the brain from harmful substances in the bloodstream, permitting only the passive diffusion of small, lipid-soluble molecules below 400–600 Da[39]. Nevertheless, particles may traverse the BBB through paracellular diffusion, transcellular transport, and transcytosis[40,41]. Moreover, PS_{20} in the brain can be rapidly cleared via the paravascular and ancillary pathways[42]. Therefore, our study indicates that only PS_{20} may be sufficiently small to cross the BBB.

Besides the tissues above, the heart, despite its central role in circulating blood[33], exhibited extremely low accumulation of PS NPs (0.0003–0.1%) (Fig. S3c), suggesting the difficulty of PS NPs to cross or adsorb on the atrial and ventricular walls. Nevertheless, a substantial amount of PS NPs was detected in other residual tissues of the rat, including skin, bone, muscle, and blood vessels (excluding the thoracic and abdominal aorta), with PS_{20} ranging from 0.23% to 23.9% and PS_{100} from 0.26% to 8.42% (Fig. S3b). The adsorption of PS NPs onto blood vessels other than the thoracic and abdominal aorta mentioned above may be an important cause for this distribution.

Maternal transfer of PS NPs via placenta and breast milk

Maternal transfer of PS NPs to offspring may take place through two primary mechanisms: translocation across the placental barrier during pregnancy and via lactation postpartum[43]. For the former, all three administration routes resulted in comparable placental accumulation of PS NPs, with PS_{20} (0.03–0.11%) showing a higher ($p < 0.05$, t-test) degree of accumulation than PS_{100} (0.005–0.044%) 1 day post administration (Fig. 4a). Further, a notable accumulation of PS_{20} (0.05–0.07%) but no PS_{100} was detected in the fetuses, indicating a size-dependent transfer of PS NPs from the placenta to the fetus (Fig. 4b).

https://doi.org/10.1038/s41467-025-67876-1

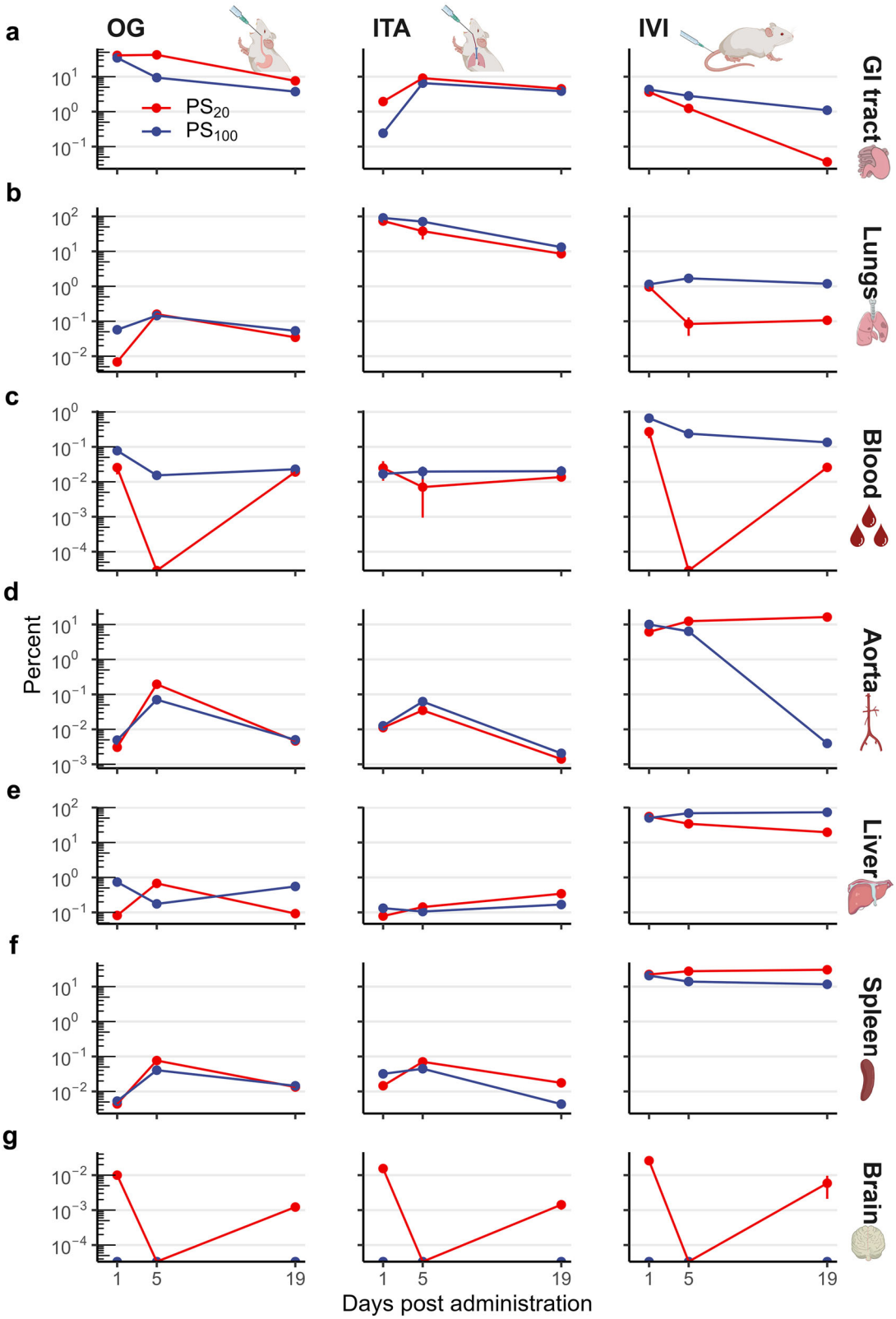

Fig. 2 | Distribution of PS NPs in different tissues and blood. The percentage of ^{14}C in the **a** gastrointestinal (GI) tract, **b** lungs, **c** blood, **d** thoracic and abdominal aorta, **e** liver, **f** spleen, and **g** brain on days 1, 5, and 19 post the administration of PS_{20} or PS_{100} via oral gavage (OG), intratracheal aerosolization (ITA), or intravenous injection (IVI). All data (mean ± standard deviation, $n = 3$) are displayed as the percentage of ^{14}C radioactivity in specific tissues or blood normalized to the total radioactivity of ^{14}C administered to the rats. Data points partially obscured below the *x*-axis represent values below the limit of quantification [(2.8×10^{-4})% of initial dose]. All data points include error bars, some of which are small and obscured by the data point symbols.

https://doi.org/10.1038/s41467-025-67876-1

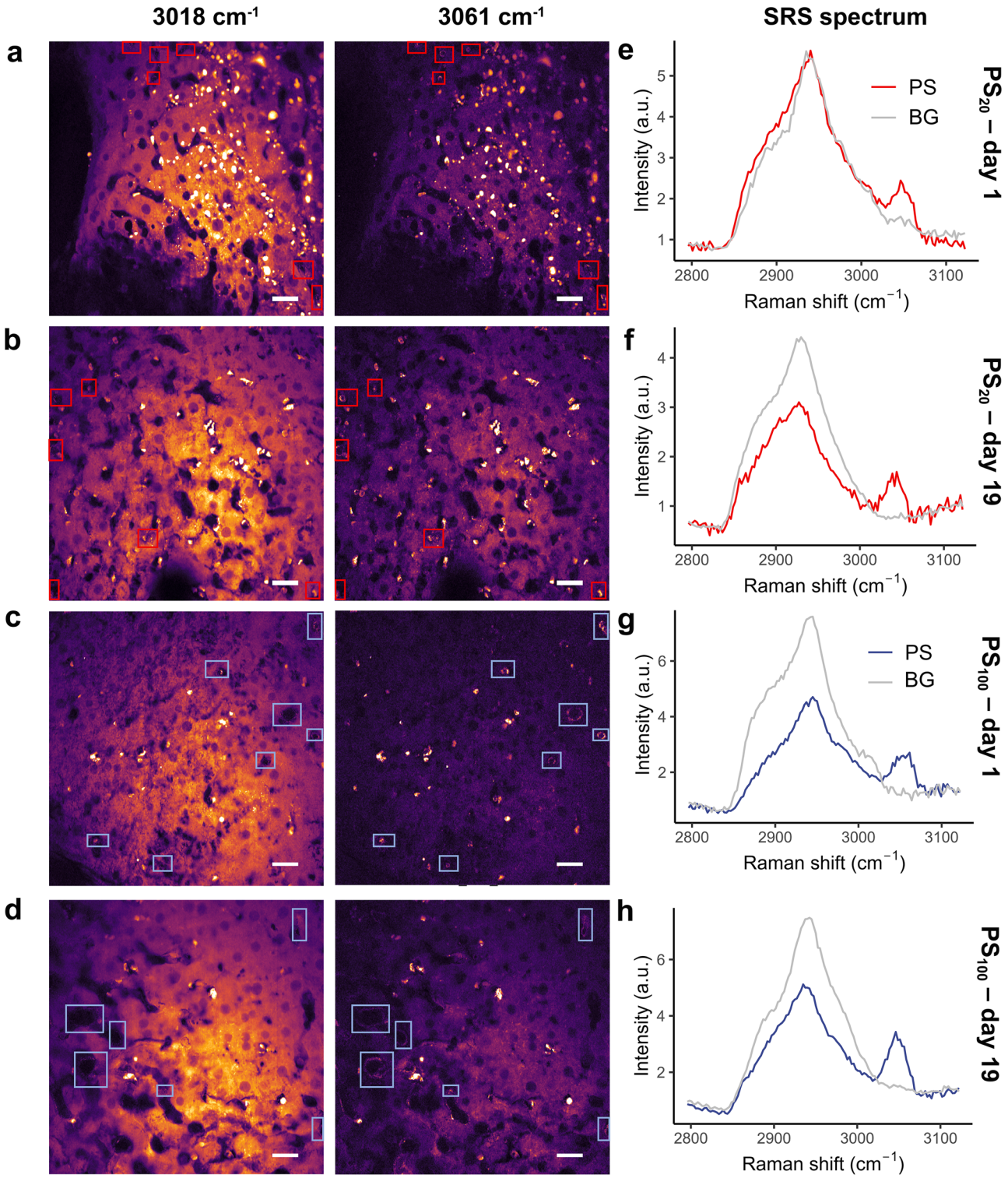

Fig. 3 | Distribution of PS NPs in the liver as imaged by SRS. The SRS signal intensity at a Raman shift of 3061 cm^{-1} (corresponding to the peak of the PS SRS spectrum) and 3018 cm^{-1} (representing the pre-peak minimum of the PS SRS spectrum) for the liver sections on days **a**, **c** 1 and **b**, **d** 19 following intravenous injection of **a**, **b** PS_{20} and **c**, **d** PS_{100}. Potential accumulation of PS_{20} and PS_{100} was highlighted within red and blue rectangles, respectively. **e**–**h** The Raman spectra of the rectangular areas in **a**–**d**, confirming the presence of PS. The Raman spectra of the tissue background (BG) were also included in **e**–**h** for comparison. The background signal intensity at 3018 cm^{-1} was higher than that at 3061 cm^{-1} due to the strong Raman signal of C-H from biomolecules (*e.g.*, lipids). Each figure was replicated in over 20 independent experiments, with similar results. Scale bars, 20 μm.

In addition to the materno-fetal transfer, a considerable presence of PS_{20} and PS_{100} was detected in rat milk (Fig. 4c). Under this condition, ~0.03–0.1% of the initial PS_{100} dose was excreted through milk 1 day postpartum (i.e., day 6 post administration in Fig. 4c), whereas the milk content of PS_{20} was significantly ($p < 0.05$, two-way ANOVA) lower at 0.003–0.005%. Moreover, the concentration of PS NPs in milk diminished rapidly over time, with no detectable NPs in milk 14 days after delivery (i.e., day 19 post administration in Fig. 4c). Comparing

https://doi.org/10.1038/s41467-025-67876-1

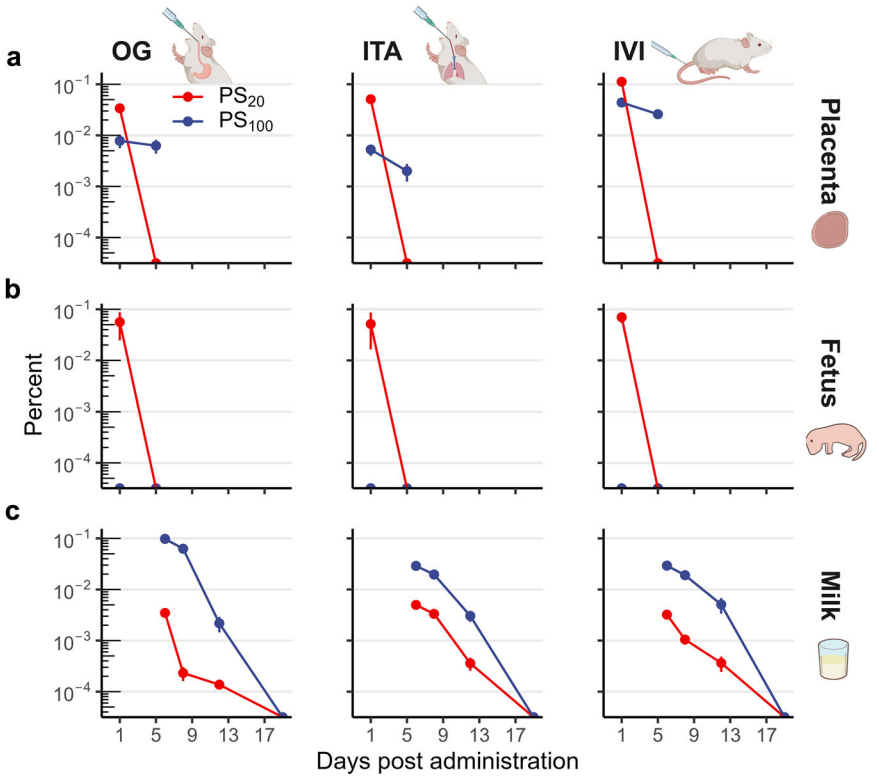

Fig. 4 | Maternal transfer of PS NPs. The percentage of ^{14}C in the **a** placenta, **b** fetus, and **c** milk on days 1–19 post the administration of PS_{20} or PS_{100} via oral gavage (OG), intratracheal aerosolization (ITA), or intravenous injection (IVI). As delivery occurred on day 5 post-administration, there are only two time points (days 1 and 5) for the distribution of PS NPs in the **a** placenta and **b** fetus. Since the *x*-axis denotes the time elapsed post-administration of PS NPs and delivery occurred on day 5 post-administration, the time points in **c** correspond to days 1, 3, 7, and 14 postpartum (*i.e.*, days 6, 8, 12, and 19 post-administration). All data (mean ± standard deviation, $n = 3$) are displayed as the percentage of ^{14}C radioactivity in the placenta, fetus, or milk normalized to the total radioactivity of ^{14}C administered to the rats. Data points partially obscured below the *x*-axis represent values below the limit of quantification [(2.8×10^{-4})% of initial dose]. All data points include error bars, some of which are small and obscured by the data point symbols.

the two maternal transfer pathways, materno-fetal transfer predominantly contributed to offspring accumulation of PS_{20}, while lactation was the only route for PS_{100} accumulation. These findings suggest that the blood-milk barrier permits a broader size range of PS NPs compared to the placental barrier[44].

PBTK modeling results of PS NP distribution in rats

To elucidate the link between external dose and internal distribution, we simulated the biodistribution and elimination data of PS NPs using a particle-based PBTK model (Figs. S4 and S5)[45]. Figure S6 shows good agreement between observed and predicted values, with most observed-to-predicted ratios within a factor of 2, indicating the model's robust predictive capacity. The derived PBTK parameters (Table S1) align with the biodistribution results of PS_{20} and PS_{100} described above. For instance, among the three administration routes, OG demonstrates the highest tissue/plasma distribution coefficient in the GI tract (P_{GI}), ITA exhibits the highest coefficient in the lung (P_{Lu}), and IVI shows the highest coefficient in the liver (P_{Li}), respectively. The substantial variation in distribution coefficients across tissues underscores their distinct permeability to PS NPs, which also depends on the administration route. A previous study[46] on PBTK modeling of PS NPs via OG reported much lower K_{Glb} ($3.4–4.2 \times 10^{-5}\,h^{-1}$) and P_{Li} (1×10^{-4}) compared to our observations ($0.02–0.17\,h^{-1}$ and 0.016–0.34). Given their data were based on positron emission tomography of ^{89}Zr-labeled PS NPs[47], our results highlight the need for reliable quantification methods to accurately predict the biological distribution of PS NPs.

In summary, the quantitative data obtained in our study reveal the critical impact of administration routes on the biodistribution of PS NPs. Notably, PS NPs administered orally were excreted in faeces, whereas those introduced intravenously accumulated predominantly in the liver and spleen, and those delivered through the respiratory tract accumulated mainly in the lungs. For orally administered PS NPs, despite rapid faecal excretion, their potential to affect the GI tract and gut microbiota warrants attention. In contrast, inhaled PS NPs require assessment of their impact on the lungs, while intravenously introduced PS NPs warrant examination of their effects on the liver and spleen. Regardless of the administration routes, we also found significant systemic accumulation of PS NPs in various tissues, indicating their ability to traverse various biological barriers in mammals. Our results underscore the need to comprehensively examine the impact of NPs across different organs and to look out for potential systemic effects. Beyond administration routes, we also found that particle size significantly influences the biodistribution of PS NPs. Of the two sizes examined, only PS_{20} may cross the BBB, potentially leading to neurotoxicity. Whereas PS_{20} were transferred maternally through both the placenta and breast milk, PS_{100} were detected only in breast milk. This differential transfer is likely to form distinct NP distribution patterns and lead to size-dependent effects in the offspring. Future research should explore the molecular mechanisms by which differently-sized PS NPs cross various biological barriers.

Although our experiments were conducted in rats, the exposure routes parallel those relevant to humans, including ingestion, inhalation, and intravenous delivery. These parallels generate testable hypotheses for human studies: ingestion-focused work should assess GI and microbiome effects, inhalation studies should examine pulmonary outcomes, and intravenous exposure studies should investigate hepatic and splenic responses. Furthermore, the evidence for

size-dependent maternal transfer highlights the need to consider vulnerable populations such as pregnant individuals, fetuses, and infants. The possibility of smaller PS NPs to cross the BBB further suggests that future human biomonitoring and risk assessments should stratify by particle size. Collectively, these translational insights emphasize the importance of investigating NP behavior under human-relevant exposure scenarios while avoiding over-extrapolation from animal data.

Method

Preparation of PS NPs and characterization

Both PS_{20} and PS_{100} were synthesized via microemulsion polymerization[26]. The process involved heating 10 mL of 1% w/v sodium dodecyl sulfate (SDS) to 67 °C, followed by the addition of 0.35 mL of ^{14}C-labeled styrene (407 MBq/g, alpha carbon labeled, Moravek, USA). After thorough mixing, 0.8 mL of 4.5% w/v potassium persulfate was added to initiate a 2-h polymerization and PS_{20} were thus obtained. Synthesis of PS_{100} followed a similar method but with a lower SDS concentration of 0.016% w/v. Unlabeled PS NPs were also synthesized following the same method. Diafiltration through a 10-kDa regenerated cellulose membrane removed any soluble impurities in the PS NPs. The hydrodynamic diameter of the PS NPs was measured by a dynamic light scattering particle sizer (Zetasizer Nano S90, Malvern, UK), their morphology visualized using transmission electron microscopy (JEM-200CX, JEOL, Japan), and their chemical composition verified through Raman (Xplora, Horiba, France) and Fourier transform infrared (FTIR, Nexus 870, Nicolet, USA) spectroscopy.

Exposure experiment

Exposure and sample collection. Fifty-four pregnant Sprague-Dawley rats (SPF grade, 11 weeks old, gestational day 15) were purchased from Nanjing Qinglongshan Biotechnology Co., Ltd [Animal Production License No. SCXK (Su) 2024-0001]. The animals were housed under controlled conditions (23–25 °C, 50–60% humidity, 12-h light/12-h dark cycle) with ad libitum access to food and water. All experimental protocols were reviewed and approved by the Animal Ethical and Welfare Committee of Nanjing University (Approval No.: IACUC-D2211002) and conducted in accordance with the 3R principles and the Regulations for the Administration of Laboratory Animals.

The 54 rats were randomly assigned to six treatments, each receiving a single dose (0.84 mg) of ^{14}C-labeled PS_{20} or PS_{100} via OG, ITA, or IVI. Single dose (acute exposure) was applied instead of multiple doses (chronic exposure) to clearly discern the distribution profile of PS NPs. The applied dose falls within the reported range for MP intake in humans[48] and the dosage (342 kBq/animal) of ^{14}C is also at the lower end of the range employed in previous rat studies[49]. Our preliminary experiments further showed that this dosage of ^{14}C-labeled PS NPs had negligible effects on the rats. ITA was selected over traditional intratracheal or intranasal instillation methods due to its closer simulation of natural inhalation processes and its reduced likelihood of direct NP migration from the nasal cavity to the laryngopharynx and subsequent entry into the GI tract. Following exposure, the rats were singly housed in metabolic cages with continuous access to food and water. The metabolic cages separated faeces and urine, with faecal pellets sliding down through a grid into a collection channel and urine being funneled into a separate receptacle to prevent cross-contamination. Their faeces and urine were collected daily. The collection containers and funnels were cleaned with tetrahydrofuran (THF) between each collection. In our preliminary experiment, THF cleaning had been found to be able to reduce the residual ^{14}C radioactivity below detection limit. This experiment spanned 19 days, with three time points (days 1, 5, and 19), two of which (days 1 and 5) preceded delivery.

At each time point, three rats from each treatment were humanely euthanized through intraperitoneal injection of pentobarbital sodium (100 mg/kg). Blood was first collected via abdominal aorta, and the blood vessel was emptied in case of cross-contamination. Afterward, various tissues, including the GI tract (esophagus, stomach, small and large intestines, and the content inside), lungs with trachea, thoracic and abdominal aorta, liver, spleen, brain, heart, kidneys, residual tissues, as well as placenta and fetus (on days 1 and 5 only), were harvested with different scissors, which were cleaned by THF before the dissection of the next rat. The aluminum foil on the lab bench was changed as well. Offspring were also collected on days 6, 8, 12, and 19 post administration (i.e., days 1, 3, 7, and 14 postpartum) for milk sampling from the stomach. All collected samples were immediately frozen in liquid nitrogen and subsequently stored at −80 °C. Prior to analysis, the samples were freeze-dried and ground into fine powders in different agate mortars (i.e., different mortars for different tissues), which was cleaned by THF at least three times between each sample.

Total radioactivity determination. A wet combustion method was used to quantify the PS NP content in the collected excreta, tissues, and body fluids. Briefly, 20 mg of freeze-dried sample powder was placed into one arm of an H-shaped glass tube, followed by the addition of 0.8 g of potassium dichromate and 10 mL of sulfuric acid. The arms of the tube were sealed with rubber stoppers, and the contents were stirred for 30 min. The tube was then autoclaved at 121 °C for 2 h and allowed to cool to room temperature. Subsequently, 1 mL of 4 M NaOH was injected into the opposite arm of the tube to capture the $^{14}CO_2$ generated. After continuous stirring for an additional 24 h, the NaOH solution was extracted and mixed with 3 mL of scintillation cocktail (Gold Star; Meridian Biotechnologies Ltd, Epsom, UK). The radioactivity of the samples was measured by liquid scintillation counting (LSC, LS6500, Beckman Coulter, Brea, USA). The PS NP content was then calculated based on the radioactivity of ^{14}C and total weight of the excreta, tissues, and body fluids. Due to the inability to collect all postpartum milk from the rats, the dry weight of milk was approximated to be 8.0 grams per day[50]. The recovery yields for the wet combustion method used to quantify ^{14}C radioactivity were 100 ± 5% (Table S2). These yields were determined using 20 mg of freeze-dried tissues or body fluids from rats not exposed to PS NPs, to which known amounts (33 Bq) of ^{14}C-labeled PS NPs were added. Moreover, the mass balance analysis showed that 91.3% to 100.8% of the initial ^{14}C dose was accounted for in excreta, tissues, and body fluids across various particle sizes and administration routes (Tables S3 and S4).

Measurement of MW distribution. The MW distribution of the ^{14}C-labeled compounds within the excreta, tissues, and body fluids was determined using GPC (PL-GPC120, Agilent Technologies, USA). For this purpose, 0.1–0.5 g of freeze-dried powder from each sample was mixed with 20 mL of THF, sonicated for 30 min, and centrifuged at 3900 × *g* for 15 min. The resulting supernatant was concentrated through rotary evaporation and then analyzed by GPC equipped with a PL-gel MIXED-C column (5 μm, 300 mm × 7.5 mm). The column was maintained at 40 °C, with THF as the mobile phase at a flow rate of 1 mL/min. Fractions were collected every 0.25 min, and the radioactivity of the eluent was determined by LSC. For reference, the MW distribution of the ^{14}C-labeled PS_{20} and PS_{100} was similarly assessed, along with that of the residual mono- and oligomers which were removed from both PS NPs via diafiltration through a 10-kDa regenerated cellulose membrane as mentioned before.

PBTK modeling of the biodistribution data of PS NPs

The biodistribution results of ^{14}C-labeled PS_{20} and PS_{100} were simulated using a particle-based PBTK model[45]. Unlike traditional PBTK models for small molecules, this particle-based approach accounts for endocytosis in tissues such as lungs, spleen, liver, and kidneys, assuming permeability-limited rather than perfusion-limited

distribution of PS NPs. Figure S4 illustrates the initial compartmentalization of rats into ten distinct compartments: lungs, spleen, liver, GI tract, kidneys, heart, brain, placenta, mammary gland, and the residual tissues. The lungs, spleen, liver, and kidneys were each further subdivided into three sub-compartments: capillary blood, tissue, and phagocytic cells (PCs). PCs are hypothesized to be the primary cells responsible for PS NP uptake, exerting a significant influence on their transport and circulation. Other organs and compartments were divided into capillary blood and tissue sub-compartments. To incorporate the administration routes of ITA and OG, the model integrated the extrathoracic region into the lung compartment and the gut lumen into the GI tract. The model also established the transfer of PS NPs between the placenta and the fetus and accounted for milk secretion in the mammary gland compartment. All compartments are interconnected through the circulatory system, with the exchange of PS NPs between blood and tissues occurring via a permeability-limited process.

The partitioning of PS NPs between capillary blood, tissues, and PCs (when applicable) within each compartment at time t was mainly characterized by the following equations,

$$\frac{dA_{blood\_com}}{dt} = Q_{com} \times (C_{art} - C_{blood\_com}) - PA_{com} \times \left(C_{blood\_com} - \frac{C_{tissue\_com}}{P_{com}}\right) \quad (1)$$

$$\frac{dA_{tissue\_com}}{dt} = PA_{com} \times \left(C_{blood\_com} - \frac{C_{tissue\_com}}{P_{com}}\right) - \left(K_{up\_com} \times A_{tissue\_com} - K_{re\_com} \times A_{PC\_com}\right) \quad (2)$$

$$\frac{dA_{PC\_com}}{dt} = K_{up\_com} \times A_{tissue\_com} - K_{re\_com} \times A_{PC\_com} \quad (3)$$

Where A_{blood_com}, A_{tissue_com}, and A_{PC_com} denote the mass (ng) of PS NPs in the capillary blood, tissues, and PCs of each compartment, respectively. C_{art} represents the concentration (ng/kg) of PS NPs in arterial blood, while C_{blood_com} and C_{tissue_com} are the mass concentrations (ng/kg) of PS NPs in the capillary blood and tissues of each compartment. Q_{com} (kg/h) signifies the blood flow rate in each compartment, P_{com} is the tissue-blood partition coefficient of each compartment, K_{up_com} (1/h) and K_{re_com} (1/h) are the uptake and release rate constants of PS NPs by PCs of the respective compartment. The permeability area cross product PA_{com} (kg/h) for each compartment is calculated as the product of Q_{com} and the permeability coefficient between capillary blood and tissue (PAC). The rats in the model had an average body weight of 0.45 kg, and the physiological parameters used for these calculations are detailed in Table S5.

The model was calibrated and differential equations were solved using SimBiology® (v24.2) within MATLAB™ 2024b (The MathWorks, Inc., Natick, MA, USA), employing the ode15s solver. Kinetic parameters were derived by fitting the data with the Fit Data function in SimBiology®, utilizing the lsqnonlin algorithm with a proportional error model. The accuracy of the PBTK model was assessed by comparing observed and predicted values.

SRS imaging

Similar to the exposure experiment above, an additional cohort of 6 rats were exposed to 0.84 mg per rat of unlabeled PS_{20} or PS_{100} via IVI in triplicate. A control treatment was also included without exposure to PS NPs. On day 1 or 19 post administration, each rat was subjected to anesthesia, followed by cannulation of the aorta through the left ventricle[51]. Subsequently, the arterial system was rapidly flushed with 150 mL of saline, after which 250 mL of a 4% paraformaldehyde solution (w/v, pH = 7.40) was perfused. The liver was then embedded in agarose, and sections of 100 μm thickness were sliced for further analysis by SRS. The ability of SRS to visualize the bioaccumulation and biodistribution of PS NPs had been verified in the previous study from our group[52].

The SRS system integrated a dual-output femtosecond (fs) laser (InSight X3, Spectra-Physics, Newport, USA), which provides pump (800 nm, ~120 fs) and Stokes (1045 nm, ~220 fs) beams with an 80 MHz repetition rate. The intensity of the 1045 nm Stokes beam was modulated by an acousto-optical modulator (1205-C, Isomet, USA) at 2.5 MHz. The pump and Stokes pulses were both chirped to ~3 ps by a 75 cm long SF57 glass rod, and were spatially overlapped by a dichroic mirror (DMSP1000L, Thorlabs, USA). The temporal overlap between pump and Stokes pulses was ensured by a time delay line in the Stokes beam. Laser beams were scanned by a two-axis galvanometer (GVS002, Thorlabs, USA) for SRS imaging. The SRS signal was detected by a photodiode and resonant amplifier, demodulated by a lock-in amplifier (HF2LI, Zurich Instruments, Switzerland) at 2.5 MHz. Imaging utilized a 60× objective (N.A. 1.2, UPLSAPO 60XW) with laser powers of 40 mW for the pump and 80 mW for the Stokes beam. The dwell time was set at 20 μs, and the field of view was 200 × 200 μm^2 with 400×400 pixels. The SRS spectra were acquired by adjusting the delay time of the Stokes laser.

Statistical analysis

Statistical analyzes were conducted to assess several key aspects of our findings, including the time-dependent distribution of PS_{20} and PS_{100}, the differences between these two size variants, and the effects of various administration routes on the biodistribution of both PS NPs. Significant differences ($p < 0.05$) were based on the results of a one-way or two-way analysis of variance with post-hoc multiple comparisons (Tukey or Tamhane; IBM SPSS Statistics 22.0, NY, USA). The normality (Kolmogorov–Smirnov and Shapiro–Wilk tests) and homogeneity of variance (Levene's test) of the data were determined during the analysis of variance. Student's t-test was used to test the significant difference between two treatments.

Reporting summary

Further information on research design is available in the Nature Portfolio Reporting Summary linked to this article.

Data availability

The data supporting the findings of this study are available within this manuscript. All other relevant data are available from the corresponding authors upon reasonable request. Source data are provided with this manuscript. Source data are provided with this paper.

References

1. Geyer, R. J., Jambeck, J. R. & Law, K. L. Production, use, and fate of all plastics ever made. *Sci. Adv.* **3**, e1700782 (2017).
2. Su, Y. et al. Steam disinfection releases micro(nano)plastics from silicone-rubber baby teats as examined by optical photothermal infrared microspectroscopy. *Nat. Nanotechnol.* **17**, 76–85 (2022).
3. Mitrano, D. M., Wick, P. & Nowack, B. Placing nanoplastics in the context of global plastic pollution. *Nat. Nanotechnol.* **16**, 491–500 (2021).
4. Revell, L. E. et al. Direct radiative effects of airborne microplastics. *Nature* **598**, 462–467 (2021).
5. Santos, R. G., Machovsky-Capuska, G. E. & Andrades, R. Plastic ingestion as an evolutionary trap: toward a holistic understanding. *Science* **373**, 56–60 (2021).
6. Vethaak, A. D. & Legler, J. Microplastics and human health. *Science* **371**, 672–674 (2021).
7. Senathirajah, K. et al. Estimation of the mass of microplastics ingested - A pivotal first step towards human health risk assessment. *J. Hazard. Mater.* **404**, 124004 (2021).

8. Zhang, J., Wang, L. & Kannan, K. Polyethylene terephthalate and polycarbonate microplastics in pet food and feces from the United States. *Environ. Sci. Technol.* **53**, 12035–12042 (2019).
9. Cohen et al. Emerging applications of stimuli-responsive polymer materials. *Nat. Mater.* **9**, 101–113 (2010).
10. Zheng, X., Feng, Q. & Guo, L. Quantitative analysis of microplastics and nanoplastics released from disposable PVC infusion tubes. *J. Hazard. Mater.* **465**, 133246 (2024).
11. Rawle, D. J. et al. Microplastic consumption induces inflammatory signatures in the colon and prolongs a viral arthritis. *Sci. Total Environ.* **809**, 152212 (2022).
12. Shiu, H. T. et al. Dietary exposure to polystyrene nanoplastics impairs fasting-induced lipolysis in adipose tissue from high-fat diet fed mice. *J. Hazard. Mater.* **440**, 129698 (2022).
13. Shen, R. et al. Accumulation of polystyrene microplastics induces liver fibrosis by activating cGAS/STING pathway. *Environ. Pollut.* **300**, 118986 (2022).
14. Xu, D., Ma, Y., Han, X. & Chen, Y. Systematic toxicity evaluation of polystyrene nanoplastics on mice and molecular mechanism investigation about their internalization into Caco-2 cells. *J. Hazard. Mater.* **417**, 126092 (2021).
15. Kwon, W. et al. Microglial phagocytosis of polystyrene microplastics results in immune alteration and apoptosis in vitro and in vivo. *Sci. Total Environ.* **807**, 150817 (2022).
16. Zhu, L. et al. Unveiling small-sized plastic particles hidden behind large-sized ones in human excretion and their potential sources. *Environ. Sci. Technol.* **58**, 27 (2024).
17. Ragusa, A. et al. Plasticenta: first evidence of microplastics in human placenta. *Environ. Int.* **146**, 106274 (2021).
18. Xu, M. et al. Size-dependent in vivo transport of nanoparticles: implications for delivery, targeting, and clearance. *ACS Nano* **17**, 20825–20849 (2023).
19. Schur, C. et al. When fluorescence is not a particle: The tissue translocation of microplastics in *Daphnia magna* seems an artifact. *Environ. Toxicol. Chem.* **38**, 1495–1503 (2019).
20. Jani, P., Halbert, G. W., Langridge, J. & Florence, A. T. Nanoparticle uptake by the rat gastrointestinal mucosa: Quantitation and particle size dependency. *J. Pharm. Pharmacol.* **42**, 821–826 (1990).
21. Im, C. et al. PET tracing of biodistribution for orally administered (64)Cu-labeled polystyrene in mice. *J. Nucl. Med.* **63**, 461–467 (2022).
22. Delaney, S. et al. Unraveling the in vivo fate of inhaled micro- and nanoplastics with PET imaging. *Sci. Total Environ.* **904**, 166320 (2023).
23. Luo, Y. et al. Quantitative tracing of uptake and transport of submicrometre plastics in crop plants using lanthanide chelates as a dual-functional tracer. *Nat. Nanotechnol.* **17**, 424–431 (2022).
24. Mitrano, D. M. et al. Synthesis of metal-doped nanoplastics and their utility to investigate fate and behaviour in complex environmental systems. *Nat. Nanotechnol.* **14**, 362–368 (2019).
25. Al-Sid-Cheikh, M. et al. Uptake, whole-body distribution, and depuration of nanoplastics by the scallop *Pecten maximus* at environmentally realistic concentrations. *Environ. Sci. Technol.* **52**, 14480–14486 (2018).
26. Al-Sid-Cheikh, M. et al. Synthesis of ^{14}C-labelled polystyrene nanoplastics for environmental studies. *Commun. Mater.* **1**, 97 (2020).
27. Clark, N. J., Fischer, A. C., Durndell, L., Galloway, T. S. & Thompson, R. C. Translocation of ^{14}C-polystyrene nanoplastics into fish during a very-low concentration dietary exposure. *Chemosphere* **341**, 140058 (2023).
28. Shelver, W. L., McGarvey, A. M., Billey, L. O. & Banerjee, A. Fate and disposition of [^{14}C]-polystyrene microplastic after oral administration to laying hens. *Sci. Total Environ.* **909**, 168512 (2024).
29. Sarin, H. Physiologic upper limits of pore size of different blood capillary types and another perspective on the dual pore theory of microvascular permeability. *J. Angiogenes Res.* **2**, 14 (2010).
30. Oliver, J. et al. Determination of glomerular size-selectivity in the normal rat with Ficoll. *J. Am. Soc. Nephrol.* **3**, 214–228 (1992).
31. Wright, S. L. & Kelly, F. J. Plastic and human health: a micro issue? *Environ. Sci. Technol.* **51**, 6634–6647 (2017).
32. Prust, M., Meijer, J. & Westerink, R. H. S. The plastic brain: neurotoxicity of micro- and nanoplastics. *Part. Fibre Toxicol.* **17**, 24 (2020).
33. Hall, C., Lueshen, E., Mosat, A. & Linninger, A. A. Interspecies scaling in pharmacokinetics: a novel whole-body physiologically based modeling framework to discover drug biodistribution mechanisms in vivo. *J. Pharm. Sci.* **101**, 1221–1241 (2012).
34. Marfella, R. et al. Microplastics and nanoplastics in atheromas and cardiovascular events. *N. Engl. J. Med.* **390**, 10 (2024).
35. Jani, P. U., McCarthy, D. E. & Florence, A. T. Nanosphere and microsphere uptake via Peyer's patches: observation of the rate of uptake in the rat after a single oral dose. *Int. J. Pharm.* **86**, 239–246 (1992).
36. Jani, P., Halbert, G., Langridge, J. & Florence, L. A. The uptake and translocation of latex nanospheres and microspheres after oral administration to rats. *J. Pharm. Pharmacol.* **41**, 809–812 (1989).
37. Smyth, S. H., Feldhaus, S., Schumacher, U. & Carr, K. E. Uptake of inert microparticles in normal and immune deficient mice. *Int. J. Pharm.* **346**, 109–118 (2008).
38. Mohammad, A. K., Amayreh, L. K., Mazzara, J. M. & Reineke, J. J. Rapid lymph accumulation of polystyrene nanoparticles following pulmonary administration. *Pharm. Res.* **30**, 424–434 (2013).
39. Zhao, Y. et al. Factors influencing the blood-brain barrier permeability. *Brain Res.* **1788**, 147937 (2022).
40. Wu, D. et al. The blood-brain barrier: structure, regulation, and drug delivery. *Signal Transduct. Target. Ther.* **8**, 217 (2023).
41. Kreuter, J. et al. Apolipoprotein-mediated transport of nanoparticle-bound drugs across the blood-brain barrier. *J. Drug Target.* **10**, 317–325 (2002).
42. Gu, X. et al. Clearance of two organic nanoparticles from the brain via the paravascular pathway. *J. Control Release* **322**, 31–41 (2020).
43. Grafmueller, S. et al. Bidirectional transfer study of polystyrene nanoparticles across the placental barrier in an ex vivo human placental perfusion model. *Environ. Health Perspect.* **123**, 1280–1286 (2015).
44. Wellnitz, O. & Bruckmaier, R. M. Invited review: The role of the blood-milk barrier and its manipulation for the efficacy of the mammary immune response and milk production. *J. Dairy Sci.* **104**, 6376–6388 (2021).
45. Chen, C. Y. & Lin, Z. Exploring the potential and challenges of developing physiologically-based toxicokinetic models to support human health risk assessment of microplastic and nanoplastic particles. *Environ. Int.* **186**, 108617 (2024).
46. Chen, C. Y., Kamineni, V. N. & Lin, Z. A physiologically based toxicokinetic model for microplastics and nanoplastics in mice after oral exposure and its implications for human dietary exposure assessment. *J. Hazard. Mater.* **480**, 135922 (2024).
47. Keinänen, O. et al. Harnessing PET to track micro- and nanoplastics in vivo. *Sci. Rep.* **11**, 11463 (2021).
48. Liu, C. et al. Widespread distribution of PET and PC microplastics in dust in urban China and their estimated human exposure. *Environ. Int.* **128**, 116–124 (2019).
49. Tian, J. et al. Absorption, distribution, metabolism, and excretion of [^{14}C]NBP (3-*n*-butylphthalide) in rats. *J. Chromatogr. B* **1181**, 122915 (2021).
50. Russell, J. A. Milk yield, suckling behaviour and milk ejection in the lactating rat nursing litters of different sizes. *J. Physiol.* **303**, 403–415 (1980).

51. Gage, G. J., Kipke, D. R. & Shain, W. Whole animal perfusion fixation for rodents. *J. Vis. Exp.* **30**, 3564 (2012).
52. Wang, M. et al. Stimulated Raman scattering microscopy reveals bioaccumulation of small microplastics in protozoa from natural waters. *Environ. Sci. Technol.* **58**, 2922–2930 (2024).

Acknowledgements

This work was supported by the National Natural Science Foundation of China (22436002), the National Key R&D Program of China (grant no. 2022YFA1205603, 2022YFC3204400, and 2023YFE0121500), and the Fundamental Research Funds for the Central Universities (021114380234).

Author contributions

A.J.M. conceived the idea, with R.J. providing additional input. H.J.Z. performed the exposure experiments. S.L. and P.W. performed the SRS experiment. H.J.Z. and Z.H. prepared the nanoplastics. H.J.Z., X.L.W., K.D.Z., W.J., and X.W. performed the GPC analysis. A.J.M., H.J.Z., H.T.F., R.J., Q.G.T., L.Y., B.P., and B.X. analyzed the data and drew the figures. A.J.M., R.J., and H.J.Z. wrote the paper with contributions from all co-authors.

Competing interests

The authors declare no competing interests.

Additional information

Supplementary information The online version contains supplementary material available at https://doi.org/10.1038/s41467-025-67876-1.

Correspondence and requests for materials should be addressed to Rong Ji, Ping Wang or Ai-Jun Miao.

Peer review information *Nature Communications* thanks the anonymous reviewers for their contribution to the peer review of this work. A peer review file is available.